



Cite this: *Green Chem.*, 2017, **19**, 2416

## Photo-assisted water oxidation by high-nuclearity cobalt-oxo cores: tracing the catalyst fate during oxygen evolution turnover†

M. Natali,<sup>a</sup> I. Bazzan,<sup>‡b</sup> S. Goberna-Ferrón,<sup>§c,d</sup> R. Al-Oweini,<sup>¶b,e</sup> M. Ibrahim,<sup>||e</sup> B. S. Bassil,<sup>\*\*e</sup> H. Dau,<sup>Ⓜf</sup> F. Scandola,<sup>a</sup> J. R. Galán-Mascarós,<sup>Ⓜc,d</sup> U. Kortz,<sup>e</sup> A. Sartorel,<sup>b</sup> I. Zaharieva<sup>Ⓜf</sup> and M. Bonchio<sup>Ⓜ\*b</sup>

Multi-nuclear cobalt cores have been proposed as molecular analogues of the natural oxygen evolving complex, enabling water oxidation for artificial photosynthesis schemes and the production of solar fuels. In particular, cobalt containing polyoxometalates (Co-POMs) display a record activity as water oxidation catalysts (WOCs) in terms of the turnover number, turnover frequency, and quantum yield, when combined in a light activated oxygen evolving cycle with Ru(bpy)<sub>3</sub><sup>2+</sup> (bpy = 2,2'-bipyridine) as the photosensitizer. The unique behavior of high-nuclearity cobalt clusters is addressed herein by employing Co-POMs with Co ≥ 9 as molecular WOCs. The temporal dissection of the catalytic events is framed herein to investigate the initial photo-induced electron transfer (ET) occurring in the micro-to-millisecond time domain, and followed by the oxygen evolution kinetics taking place within a minute-to-hours regime. In particular, flash photolysis shows ET from the Co-POM to photogenerated Ru(bpy)<sub>3</sub><sup>3+</sup> with well-behaved diffusional kinetics (bimolecular rate constants in the range  $k_{ET} = 2.1\text{--}5.0 \times 10^9 \text{ M}^{-1} \text{ s}^{-1}$ ) and counting up to 32 ET events in a 60 ms timeframe. The evolution of the Co-POMs is then traced under oxygenic conditions, where infrared and X-ray absorption spectroscopy (XAS) indicate that POM based structures are competent catalysts under the photo-assisted turnover regime.

Received 5th January 2017,  
Accepted 13th March 2017

DOI: 10.1039/c7gc00052a

rs.c.li/greenchem

<sup>a</sup>Department of Chemical and Pharmaceutical Sciences, University of Ferrara, Via Fossato di Mortara 17-19, and Centro Interuniversitario per la Conversione Chimica dell'Energia Solare (SolarChem), sez. di Ferrara, via L. Borsari 46, 44121 Ferrara, Italy

<sup>b</sup>Department of Chemical Sciences University of Padova and Institute on Membrane Technology, Unit of Padova, via F. Marzolo 1, 35131 Padova, Italy.  
E-mail: marcella.bonchio@unipd.it

<sup>c</sup>Institute of Chemical Research of Catalonia (ICIQ), The Barcelona Institute of Science and Technology (BIST), Av. Paisos Catalans, 16, E-43007 Tarragona, Spain

<sup>d</sup>ICREA, Passeig Lluís Companys, 23, E-08010 Barcelona, Spain

<sup>e</sup>Jacobs University, Department of Life Sciences and Chemistry, Campus Ring 1, 28759 Bremen, Germany

<sup>f</sup>Freie Universität Berlin, FB Physik, Arnimallee 14, 14195 Berlin, Germany

† Electronic supplementary information (ESI) available: Conductometric titrations, pulsed emission experiments, laser flash photolysis, UV-vis analysis of reaction mixtures, infrared spectroscopy, EXAFS spectroscopy. See DOI: 10.1039/c7gc00052a

‡ Current address: Institut Lavoisier de Versailles, UMR 8180, Université Paris-Saclay, Université de Versailles Saint-Quentin en Yvelines, 45 Avenue des Etats-Unis, 78035 Versailles cedex, France.

§ Current address: ESRF—The European Synchrotron, 71 Avenue des Martyrs, 38000 Grenoble, France.

¶ Current address: Department of Chemistry, Faculty of Science, Beirut Arab University P.O. Box 11 50 20, Riad El Solh 1107 2809 Beirut, Lebanon.

|| Current address: Institute of Nanotechnology, Karlsruhe Institute of Technology (KIT), Hermann-von-Helmholtz Platz 1, 76344 Eggenstein-Leopoldshafen, Germany.

\*\* Current address: Department of Chemistry, Faculty of Sciences, University of Balamand, P. O. Box 100, Tripoli, Lebanon.

## Introduction

Solar water splitting into O<sub>2</sub> and H<sub>2</sub> has the potential to solve the renewable energy impasse, albeit posing one formidable chemical challenge, *i.e.* the multi-electron oxidation of water which is still the crucial bottleneck of the overall process.<sup>1</sup> The long-sought goal is the discovery of a cost-effective water oxidation catalyst (WOC)<sup>2</sup> enabling O<sub>2</sub> evolution using visible light irradiation while offering multi-turnover performance, long term stability, and sustainable wide distribution and availability implemented by the use of “earth-abundant” transition metals.

Indeed, Nature has evolved a unique tetra-manganese cluster, embedded in photosystem II enzymes (PSII), that is responsible for photo-induced water oxidation and provides the chemical engine for all photosynthetic organisms.<sup>3</sup> Therefore, synthetic WOCs have been conceived along bio-inspired guidelines, by a tailored design of multi-redox transition metal manifolds that can oxidize water and evolve oxygen *via* a stepwise, light-activated mechanism. While the complexity of the photo-assisted mechanism depends on the catalytic routine and is hardly described by one single scenario, two key events are typically comprised at the start and closing of the oxygen evolution cycle:

(i) a luminous phase taking place by a sequence of photo-induced electron transfer (ET) events, through which the catalyst reaches a high-valent (oxidized) reactive state, upon multi-“hole” accumulation;

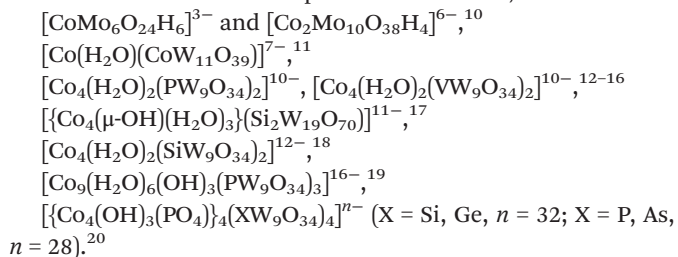
(ii) a dark phase of oxygen release which restores the catalyst in its resting (reduced) state, and guarantees catalytic turnover.

Photo-induced ET is expected to take place in the first few steps of the catalytic regime by fast events, occurring in the micro-to-milliseconds time domain. In contrast, the dark chemical transformations dictate the slow oxygen evolution kinetics and turnover frequency (TOF), spanning from a second-to-hour temporal window.

The photocatalytic system is thus exposed to alternating light-induced/dark-phase phenomena, where stability and/or structural dynamics regulate the overall turnover performance. Modification of the catalyst structure during the turnover regime, spanning diverse time-boundaries, is indeed one major issue of solar water splitting in both natural and artificial systems. Aiming at the WOC upgrade, the identification of the competent species, generated from the catalyst initial state, is instrumental to draw any possible structure–reactivity relationships. In this quest polyoxometalates (POMs) have been proposed as the structural analogues of the natural PSII cluster, thus providing a functional model of the photo-activated cycle *in vitro*.<sup>4–6</sup>

POMs are a versatile family of catalysts exhibiting a nano-dimensional but molecular metal–oxide structure, that can be tuned to integrate multi-nuclear WOC cores.<sup>4,5</sup> Cobalt containing POMs are among the most promising ones<sup>6</sup> *vis-à-vis* the imperative goal of a sustainable energy economy and “green” catalysis avoiding the use of rare and expensive noble-metals. Moreover, the toxicity of Co-POMs has been addressed in aqueous solution and depends on the concentration conditions and the time of exposure, as demonstrated in the case of  $[\text{Co}_4(\text{H}_2\text{O})_2(\text{PW}_9\text{O}_{34})_2]^{10-}$ .<sup>6b</sup> It is noteworthy that its encapsulation into a carboxymethyl chitosan matrix is instrumental to override the toxicity effects.<sup>6b</sup> This observation highlights the key importance of a tailored material choice for the upgrade to energy devices.<sup>7</sup>

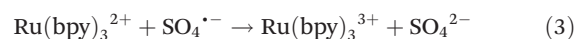
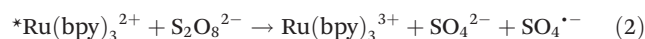
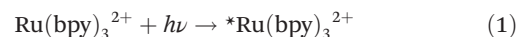
The POM structure is shaped to encapsulate a discrete cobalt–oxide fragment, so as to provide a molecular equivalent of amorphous cobalt oxide phases,<sup>8,9</sup> albeit with an improved stability in water, featuring a highly hydrophilic and electron-withdrawing POM environment. Several POM-based platforms have been described to incorporate cobalt WOCs, with formulae:



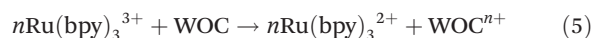
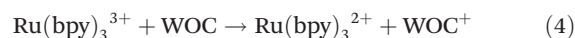
Among them, cobalt oxide clusters with a high nuclearity have shown an increased stability at neutral pH, and could be

dispersed within a solid state matrix.<sup>21</sup> Thus, they are particularly promising for their implementation into functional water photo-splitting schemes. In this case, the POM based WOC is generally used in combination with  $\text{Ru}(\text{bpy})_3^{2+}$  (bpy = 2,2'-bipyridine) as the photosensitizer and in the presence of sodium persulfate,  $\text{S}_2\text{O}_8^{2-}$  as a sacrificial electron acceptor, giving rise to a cascade of events spanning a time sequence from nano-seconds to hours, as described by eqn (1)–(6).<sup>5</sup>

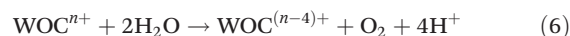
Photogeneration of  $\text{Ru}(\text{bpy})_3^{3+}$  as an oxidant (nanoseconds)



Hole accumulation by ET from WOC to  $\text{Ru}(\text{bpy})_3^{3+}$  (micro-to-milli-seconds)



Water oxidation and oxygen evolution (minutes-to-hours)



Within these reaction schemes, the POM activity is readily assessed on the basis of the primary photo-induced ET events, leading to WOC oxidation (eqn (4) and (5)). In view of this, laser flash photolysis studies, monitoring photoinduced ET from the POM donor, have been proposed as functional probes to evaluate the POM behaviour in the micro-second time domain and to sort out the initial decomposition issues.<sup>5,22–24</sup> For instance, diffusional ET occurring within a bimolecular POM-sensitizer, donor–acceptor interaction ( $k_{\text{ET}} = 3.6 \times 10^9 \text{ M}^{-1} \text{ s}^{-1}$ ), has been observed for a tetra-ruthenium polyoxotungstate, namely  $\{\text{Ru}_4\text{O}_4(\mu\text{-OH})_2(\text{H}_2\text{O})_4[\gamma\text{-SiW}_{10}\text{O}_{36}]\}^{10-}$ .<sup>22</sup>

Herein we compare and contrast the activity of  $[\text{Co}_9(\text{H}_2\text{O})_6(\text{OH})_3(\text{PW}_9\text{O}_{34})_3]^{16-}$  ( $\text{Co}_9$ ),<sup>25</sup>  $[\text{Co}_6(\text{H}_2\text{O})_{30}\{\text{Co}_9\text{Cl}_2(\text{OH})_3(\text{H}_2\text{O})_9(\text{SiW}_8\text{O}_{31})_3\}]^{5-}$  ( $\text{Co}_{15}$ )<sup>26</sup> and  $[\{\text{Co}_4(\text{OH})_3(\text{PO}_4)_4\}(\text{PW}_9\text{O}_{34})_4]^{28-}$  ( $\text{Co}_{16}$ )<sup>27</sup> (Fig. 1) along a photocatalytic cycle with  $\text{Ru}(\text{bpy})_3^{2+}$  ultimately evolving oxygen from water (eqn (1)–(6)). Our results include the dissection of the light-phase, by investigating the photo-induced ET kinetics from few  $\mu\text{s}$  to tens of ms, and the following dark-catalysis from minutes to several hours when oxygen evolution is observed.

In particular, we highlight the key role of the polyoxotungstate platform, binding the cobalt-oxo domains to leverage fast and multiple electron transfers to photogenerated  $[\text{Ru}(\text{bpy})_3]^{3+}$  (eqn (4) and (5)). Optimization of the light-to-catalyst interface is one key target to enhance the photo-conversion efficiency towards sustainable energy schemes. The POM-based innovation can exploit a favorable interplay of electrostatic association forces and hydrogen-bonded networks, that cooperate in the self-assembly of the photosynthetic unit. This is one key point of advancement with respect to the vast literature on covalently linked dyads,<sup>28</sup> generally affected by major recombina-

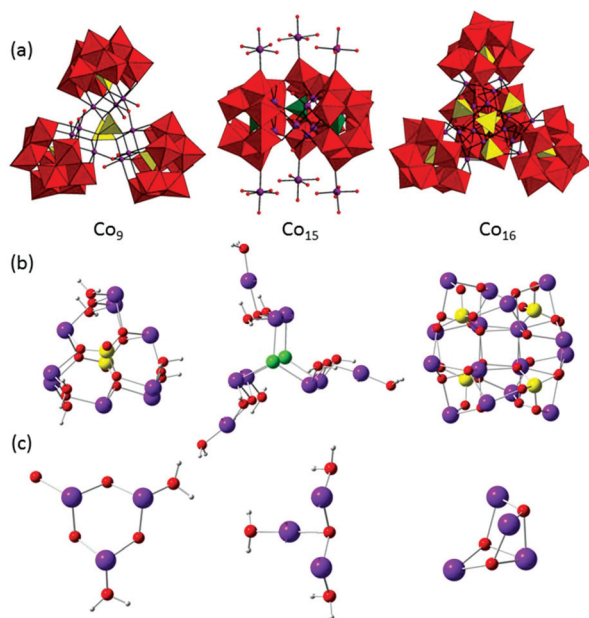


**Fig. 1** Combined polyhedral/ball and stick representation of (a)  $\text{Co}_9$ ,  $\text{Co}_{15}$  and  $\text{Co}_{16}$  POMs (b) the corresponding multi-cobalt cores and (c) the cobalt core building-block. Color code:  $\text{WO}_6$  octahedra in red,  $\text{PO}_4$  tetrahedra in yellow,  $\text{SiO}_4$  tetrahedra in green; P atoms in yellow, Co atoms in violet, Cl atoms in green, O atoms in red, H atoms in white (not shown in  $\mu\text{-OH}$  bridges for clarity reasons).

tion pathways and therefore unable to exploit the charge-separation state for any significant catalytic transformation. Our results set an informative structural–reactivity study on high nuclearity Co-oxo phases (number of Co atoms  $\geq 9$ ), confined by rigid and highly hydrophilic POM cages, which impart a definite, nano-topology of the catalytic site. It is noteworthy that the molecular nature of the POM catalytic core allows for a precise mapping of its evolution under photo-assisted water oxidation, as probed herein by X-ray Absorption Spectroscopy (XAS).

## Results and discussion

### Structural features of Co-POMs

As a common feature, these polyanions display a discrete multi-nuclear  $\text{Co(II)}$  core, where the metal ions are connected by bridging ligands, namely oxo, hydroxo, hydrogenophosphato, phosphato and/or chloro ligands (Fig. 1 and Table 1). The oxygen evolving cores, with a related structure, have been identified as the reactive sites of cobalt(II,III) oxides, that retain a high appeal and are among the state-of-the-art catalysts for water oxidation.<sup>8,9,29,30</sup> For these latter ones, only 1% of cobalt sites within the bulk material accounts for the observed WOC activity, which turns out to be highly sensitive to surface modifications and structural defects.<sup>30</sup> In particular a di-nuclear  $\{\text{Co}_2\text{O}_2\}$  unit has been identified as the minimal functional building block of the cobalt core, including  $\{\text{Co}_4\text{O}_6\}$  cubanes

**Table 1** Structural features of POM-embedded multi-cobalt cores under investigation (see Fig. 1)

Co-POM (charge)	Description of cobalt core	Bridging ligands	Terminal waters
$\text{Co}_9$ (16–)	<b>Three</b> $\{\text{Co}_3(\mu\text{-OH})_3(\text{H}_2\text{O})_2\}$ <b>triads</b>	3 $\text{OH}^-$ , 2 $\text{HPO}_4^{2-}$	6
$\text{Co}_{15}$ (5–)	<b>Three</b> $\{\text{Co}_3(\mu\text{-OH})(\text{H}_2\text{O})_3\}$ <b>triads</b>	2 $\text{Cl}^-$ , 3 $\text{OH}^-$	9
$\text{Co}_{16}$ (28–)	<b>Four</b> $\{\text{Co}_4(\mu\text{-OH})_3\}$ distorted <b>cubanes</b>	12 $\text{OH}^-$ , 4 $\text{PO}_4^{3-}$	—

or extended polymers.<sup>29</sup> As a general feature, a high degree of oxygen vacancy, and therefore the availability of water coordination sites, turns out to be a key effector for the WOC performance.<sup>30</sup> Indeed, when the redox-active metal site is associated with terminal aqua or hydroxo ligands, the occurrence of proton-coupled electron transfer (PCET) events favors the formation of high-valent metal–oxo intermediates by low-energy pathways, being at the turning point for the efficient use of visible light irradiation, fast turnover frequency and long-term operation stability.

Table 1 collects the main structural features of the cobalt cores and of surface sites, ascribed to the selected Co-POMs under investigation (Fig. 1), highlighting the minimal cluster composition (triads or cubanes of connected cobalt ions), their bridging units, the presence of “outer-core” cobalt sites, and the number of terminal aqua-ligands as a direct probe of the WOC open coordination sites.

In particular:

- $\text{Co}_9$  displays a cobalt core, with the formula  $\{\text{Co}_9(\mu\text{-OH})_3(\text{H}_2\text{O})_6(\text{HPO}_4)_2\}$ , composed of three  $\{\text{Co}_3(\mu\text{-OH})_3(\text{H}_2\text{O})_6\}$  triads connected through two  $\text{HPO}_4^{2-}$  bridges, with a triangle of triangles arrangement, and six terminal water molecules.

- $\text{Co}_{15}$  displays a cobalt core, with the formula  $\{\text{Co}_9(\mu\text{-OH})_3(\text{H}_2\text{O})_9\text{Cl}_2\}$ , composed of three  $\{\text{Co}_3(\mu\text{-OH})(\text{H}_2\text{O})_3\}$  triads connected through two  $\text{Cl}^-$  bridges, and six “outer-core” satellite  $\text{Co}(\text{H}_2\text{O})_5$  groups, bound to terminal oxo groups of the POM surface.<sup>26</sup> †† In  $\text{Co}_{15}$ , a total of 39 terminal water ligands are bound to cobalt centres, 9 to the nonanuclear core, and 30 to the satellite cobalt atoms.

- $\text{Co}_{16}$  displays a cobalt core, with the formula  $\{\text{Co}_{16}(\mu\text{-OH})_{12}(\text{PO}_4)_4\}$ , composed of four  $\{\text{Co}_4(\mu\text{-OH})_3\}$  distorted cubanes connected through the four phosphate moieties.<sup>20,27</sup> †† No water molecules are found as terminal ligands of the cobalt core, so that its WOC performance has to

†† These six  $\text{Co}(\text{H}_2\text{O})_5$  groups, although linked by a single oxygen bridge to the POM cage and therefore possibly susceptible to detachment from it, play an important role in stabilizing the structure, by reducing the overall negative charge of the polyanion and it was demonstrated that these external cobalt ions are not labile in solution.<sup>26a</sup>

‡‡ Alternatively, this core was described as a central  $\{\text{Co}_4\text{O}_4\}$  cubane unit, where oxygen atoms are shared with four phosphate groups, and capped by four tricovalent  $\{\text{Co}(\mu_2\text{-OH})_3\}$  units.

be ascribed to substitution equilibria likely involving the phosphate groups.<sup>20</sup>

These Co-POMs are soluble in aqueous solution where their molecular structure is maintained as confirmed by convergent techniques.<sup>19–21,25–27</sup> In particular, solution equilibria likely involving the leaching of paramagnetic Co(II) aqua ions have been addressed by means of <sup>31</sup>P-NMR line broadening analysis<sup>31</sup> under the conditions employed for the photocatalytic studies (20 mM phosphate buffer, pH 8, Fig. S1†). In these experiments, the full width at half maximum (FWHM) registered for the <sup>31</sup>P NMR signal of the phosphate buffer provides a direct estimate of the Co(II) aquo-ions' concentration, calibrated in the range 0–12.5 μM (Fig. S1†). In particular, for [Co<sub>15</sub>] = 17 μM, a [Co(II)] = 16 ± 1 μM is estimated as the upper limit of cobalt leaching, §§ corresponding to the release of one satellite cobalt center, and to a maximum of *ca.* 6% leaching of the total cobalt amount. Under analogous conditions, the cobalt leaching of Co<sub>9</sub> and Co<sub>16</sub> falls below the analysis detection limit, being detected only at a higher Co-POM concentration, where [Co<sub>9</sub>] = 110 μM yields [Co(II)] = 11 ± 0.6 μM and [Co<sub>16</sub>] = 62 μM yields [Co(II)] < 1 μM, corresponding respectively to 1% and <0.1% leaching of the total cobalt amount.

### Ru(bpy)<sub>3</sub><sup>2+</sup>/Co-POMs ion pairs

The polyanionic nature of polyoxometalates has important implications for association equilibria involving cationic photosensitizers. The formation of ion pairs is responsible for the direct quenching of the photosensitizer excited state by the associated POM,<sup>5,22–24,32,33</sup> resulting in a major decrease of the photosensitizer emission, thus competing with the oxidant photogeneration step (eqn (2)).<sup>5,22b,32</sup> Conductometric titrations show the formation of ion pairs between Ru(bpy)<sub>3</sub><sup>2+</sup> and the Co-POMs under investigation in water (Fig. S2–S4 in the ESI†). In all cases, the equivalence point corresponds to the expected charge balance ratio (Ru(bpy)<sub>3</sub><sup>2+</sup>/Co-POM = 1:8, 1:2.5 and 1:14, respectively for Co<sub>9</sub>, Co<sub>15</sub> and Co<sub>16</sub>). The impact of ion pair formation on the photosensitizer emission has been verified by fluorescence quenching experiments (Fig. 2). Indeed, Ru(bpy)<sub>3</sub><sup>2+</sup> emission (50 μM in water) is remarkably abated upon addition of equimolar Co-POMs (compare black and red traces in Fig. 2). The residual emission (see, *e.g.*, red traces in Fig. 2a and c) is also appreciably red-shifted (*ca.* 10 nm) in the presence of the Co-POM, thus suggesting a substantial electronic interaction between the Ru(bpy)<sub>3</sub><sup>2+</sup> sensitizer and the Co-POM, which further confirms the occurrence of ion-pair equilibria. Pulsed emission experiments show that the Ru(bpy)<sub>3</sub><sup>2+</sup> excited state has a constant lifetime, and confirm the occurrence of static quenching within ion pairs (Fig. S5 in the ESI†). Interestingly, the decrease of Ru(bpy)<sub>3</sub><sup>2+</sup> emission, induced by Co-POMs, is observed in the range Co<sub>16</sub> (70% abatement) > Co<sub>9</sub> (55%) > Co<sub>15</sub> (10%) and reflects the overall negative charge of the poly-

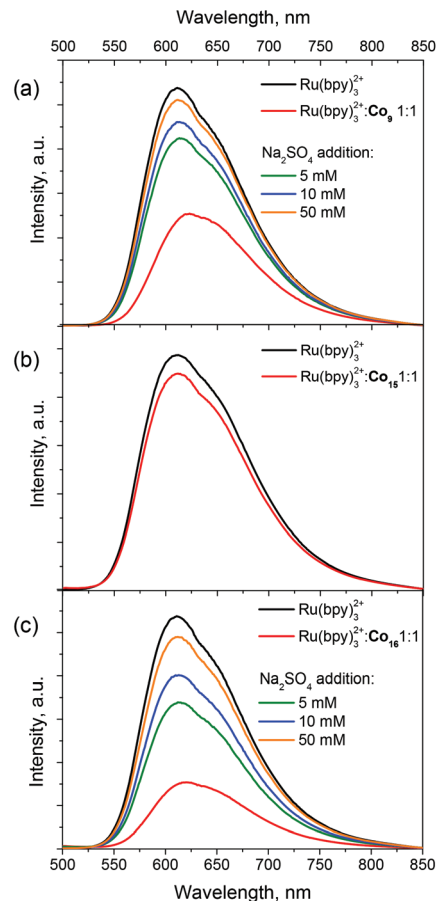


**Fig. 2** Variation of Ru(bpy)<sub>3</sub><sup>2+</sup> photoluminescence (50 μM, air-equilibrated water solution, excitation at 450 nm) upon addition of Co<sub>9</sub> (a), Co<sub>15</sub> (b) and Co<sub>16</sub> (c). Black traces: Ru(bpy)<sub>3</sub><sup>2+</sup> (reference); red traces: Ru(bpy)<sub>3</sub><sup>2+</sup> : Co-POM 1 : 1; green, blue, orange traces: Ru(bpy)<sub>3</sub><sup>2+</sup> : Co-POM 1 : 1 in the presence of 5–50 mM Na<sub>2</sub>SO<sub>4</sub>.

anion as the main driving force for the ion pair association. Indeed, buffering of the ionic strength by addition of sodium sulfate (5–50 mM) to Ru(bpy)<sub>3</sub><sup>2+</sup>/Co<sub>16</sub> and Ru(bpy)<sub>3</sub><sup>2+</sup>/Co<sub>9</sub> solutions, leads in both cases to >85% recovery of the photosensitizer emission and to the concomitant blue-shift of the luminescence maxima (green, blue and orange traces in Fig. 2a and c). It is noteworthy that the use of a 50 mM phosphate buffer (pH 8) favors a loose Ru(bpy)<sub>3</sub><sup>2+</sup>/Co-POM electrostatic interaction, which maintains the Ru(bpy)<sub>3</sub><sup>2+</sup> emission under photo-assisted catalysis (Fig. S6 in the ESI†). This is instrumental in preventing a competitive quenching of the Ru(bpy)<sub>3</sub><sup>2+</sup> excited state by Co-POMs as an alternative to the primary oxidative step with S<sub>2</sub>O<sub>8</sub><sup>2-</sup> (eqn (1)–(3) of the photo-assisted catalytic cycle).

### Hole scavenging events and kinetics

According to the persulfate sacrificial cycle, the photogeneration of Ru(bpy)<sub>3</sub><sup>3+</sup> occurs by the direct oxidative quenching of the Ru(bpy)<sub>3</sub><sup>2+</sup> excited state, and by a dark reaction of its ground state with a photo-generated sulfate radical (eqn (1)–

§§ Broadening of the <sup>31</sup>P NMR signal relative to the phosphate buffer may also arise from paramagnetic Co-POMs.



(3)). Under these conditions, the maximum value of quantum yield is 2 as two molecules of  $\text{Ru}(\text{bpy})_3^{3+}$  are possibly generated upon absorption of one photon.<sup>5,34</sup> The photogeneration of  $\text{Ru}(\text{bpy})_3^{3+}$  is confirmed by the prompt bleaching of the  $\text{Ru}(\text{bpy})_3^{2+}$  ground state ( $\lambda = 450 \text{ nm}$ ), registered under laser flash photolysis conditions (Fig. 3). These studies are of particular interest as they provide direct evidence of the multi-hole scavenging occurring in the presence of the selected Co-POM (oxidation of the Co-POM by photogenerated  $\text{Ru}(\text{bpy})_3^{3+}$ , eqn (4) and (5)). The key information is twofold: (i) the kinetics of the primary hole-scavenging event, occurring by photo-induced ET from the Co-POM donor; (ii) the number of hole-scavenging events, corresponding to the number of electrons removed from the Co-POM donor, and stimulated by photo-irradiation in a millisecond temporal window. The rate of the primary hole scavenging event under photoirradiation conditions (eqn (4)) ranks the potential WOCs, in terms of slow or fast donors with respect to  $\text{Ru}(\text{bpy})_3^{3+}$ . Slow hole scavenging WOCs (millisecond time scale) are responsible for the accumulation of  $\text{Ru}(\text{bpy})_3^{3+}$  and for its irreversible oxidative degradation, as in the case of Ir-oxide colloids.<sup>35</sup> POM-based WOCs provide the fastest hole scavenging processes known to date (microsecond time scale), showing well-behaved kinetics and multiple electron transfer efficiencies.<sup>5,22–24</sup>

Nanosecond flash photolysis was used to probe the high nuclearity cobalt POMs under photo-induced ET conditions, upon generation of  $\text{Ru}(\text{bpy})_3^{3+}$  with sodium persulfate, and by monitoring the  $\text{Ru}(\text{bpy})_3^{2+}$  bleach recovery over time, (recovery

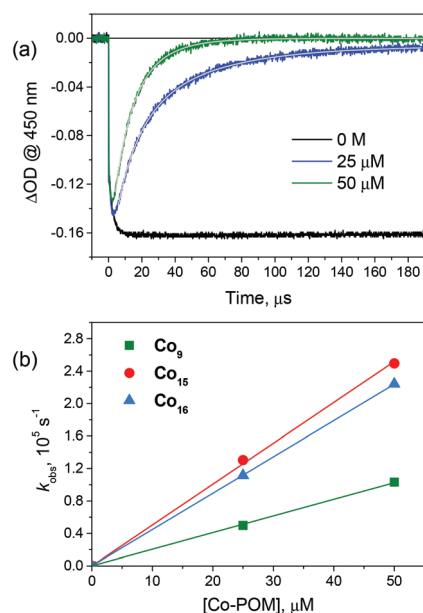


**Fig. 3** (a) Laser flash photolysis experiments ( $\lambda_{\text{exc}} = 355 \text{ nm}$ ) in aqueous phosphate buffer (pH 8) containing  $5 \text{ mM S}_2\text{O}_8^{2-}$ ,  $50 \mu\text{M Ru}(\text{bpy})_3^{2+}$ , and  $0\text{--}50 \mu\text{M Co}_9$ . (b) Plots of pseudo-first-order rate constants of bleach recovery vs. catalyst concentration, yielding bimolecular hole scavenging rate constants of  $2.1 \times 10^9$ ,  $5.0 \times 10^9$  and  $4.5 \times 10^9 \text{ M}^{-1} \text{ s}^{-1}$  for  $\text{Co}_9$ ,  $\text{Co}_{15}$  and  $\text{Co}_{16}$ , respectively.

**Table 2** Hole scavenging parameters of Co-POMs in aqueous phosphate buffer (pH 8),  $\lambda_{\text{exc}} = 355 \text{ nm}$  containing  $5 \text{ mM S}_2\text{O}_8^{2-}$ ,  $50 \mu\text{M Ru}(\text{bpy})_3^{2+}$ , and  $0\text{--}100 \mu\text{M Co-POMs}$

Co-POM	$k^a/10^9 \text{ M}^{-1} \text{ s}^{-1}$	$n(\text{ET})^b$	Redox steps <sup>c</sup>
$\text{Co}_9$	$2.1 \pm 0.3$	7.5	0.8
$\text{Co}_{15}$	$5.0 \pm 0.4$	32	2.1
$\text{Co}_{16}$	$4.5 \pm 0.4$	20	1.2

<sup>a</sup> Second order kinetic constant for the primary hole scavenging of photo-generated  $\text{Ru}(\text{bpy})_3^{3+}$  by Co-POMs ( $\lambda_{\text{exc}} = 355 \text{ nm}$  in aqueous phosphate buffer pH 8 containing  $5 \text{ mM S}_2\text{O}_8^{2-}$ ,  $50 \mu\text{M Ru}(\text{bpy})_3^{2+}$ , and  $0\text{--}100 \mu\text{M Co-POM}$ , see Fig. 3 and S6). <sup>b</sup> Number of photo-induced ET events calculated from bleach recovery occurring in 60 ms as  $[\text{Ru}(\text{bpy})_3^{2+}]/[\text{Co-POMs}]$  ( $\lambda_{\text{exc}} = 355 \text{ nm}$  in aqueous phosphate buffer pH 8 containing  $5 \text{ mM S}_2\text{O}_8^{2-}$ ,  $50 \mu\text{M Ru}(\text{bpy})_3^{2+}$ , and Co-POM with a total Co concentration of  $8\text{--}9 \mu\text{M}$ , see Fig. 4). <sup>c</sup> Average oxidation equivalents per cobalt center calculated as  $n(\text{ET})/\text{number of cobalt sites}$ .

of the metal-to-ligand-charge-transfer absorption, MLCT, at  $\lambda_{\text{max}} 450 \text{ nm}$ ) in a relatively wide window ( $0\text{--}60 \text{ ms}$ ).¶¶¶

The flash photolysis (excitation at  $\lambda 355 \text{ nm}$ ,  $8 \text{ ns}$  pulses) of  $\text{Ru}(\text{bpy})_3^{2+}$  ( $50 \mu\text{M}$ ) and  $\text{Na}_2\text{S}_2\text{O}_8$  ( $5 \text{ mM}$ ) in aqueous phosphate buffer, pH 8, shows a fast bleach (negative  $\Delta\text{OD}$ , black trace in Fig. 3) persisting in the timescale of the experiment of  $200 \mu\text{s}$ , and indicative of the  $\text{Ru}(\text{bpy})_3^{3+}$  photogeneration. Bleach recovery, associated with its back reduction to  $\text{Ru}(\text{bpy})_3^{2+}$ , is obtained upon addition of increasing concentrations of the Co-POM. The representative kinetics are shown for  $\text{Co}_9$  in Fig. 3 (see Fig. S7 in the ESI† for  $\text{Co}_{15}$  and  $\text{Co}_{16}$  kinetics). Under pseudo-first-order conditions (excess  $\text{Co}_9$  over photogenerated  $\text{Ru}(\text{bpy})_3^{3+}$ ), fitting of the recovery traces yields bimolecular rate constants which are associated with the primary hole scavenging event by the WOC (eqn (4)). For the Co-POMs investigation, the resulting second order rate constants are exceptionally high, within one order of magnitude of diffusion-controlled rates, with values of  $2.1 \pm 0.3 \times 10^9$ ,  $5.0 \pm 0.4 \times 10^9$ ,  $4.5 \pm 0.4 \times 10^9 \text{ M}^{-1} \text{ s}^{-1}$  respectively found for  $\text{Co}_9$ ,  $\text{Co}_{15}$  and  $\text{Co}_{16}$  (Fig. 3b and Table 2). These kinetic rate constants are roughly proportional to the number of cobalt atoms of the Co-POMs, suggesting that the electron transfer to  $\text{Ru}(\text{bpy})_3^{3+}$  originates from the Co(II) atoms evolving to Co(III), and occurring with a favorable thermodynamic driving force. This is confirmed by cyclic and square-wave voltammetry (Fig. S8 and S9,† respectively) of the Co-POMs showing the anodic processes relative to the  $\text{Co}^{\text{III/II}}$  couples in the potential range  $E \sim 0.80\text{--}1.00 \text{ V vs. Ag/AgCl}$  (for  $\text{Ru}(\text{bpy})_3^{3+/2+}$   $E = 1.06 \text{ V vs. Ag/AgCl}$ ).¶¶¶ Moreover, the hole-scavenging rate

¶¶ Typically, the primary formation of  $[\text{Ru}(\text{bpy})_3]^{3+}$  (eqn (1) and (2)) takes place within the time resolution of the experiment ( $10 \text{ ns}$ ) while the secondary formation by reaction with the sulfate radical (eqn (3)) in *ca.*  $5 \mu\text{s}$ .

¶¶¶ In the case of  $\text{Co}_9$  the anodic process associated with the  $\text{Co}(\text{III})/\text{Co}(\text{II})$  redox couple occurs at potentials close to the catalytic water oxidation discharge and it is not detected by square-wave voltammetry (SWV), see ref. 19a. Electrochemical analysis of the Co-POMs in non-aqueous medium (*i.e.*  $\text{CH}_3\text{CN}$ ) is generally performed by counterion metathesis with tetra-alkylammonium salts that may affect the POM stability in organic solvents. Moreover, non-aqueous media rule out access to proton coupled electron transfer events that are key features for the water oxidation mechanism by cobalt catalysts.

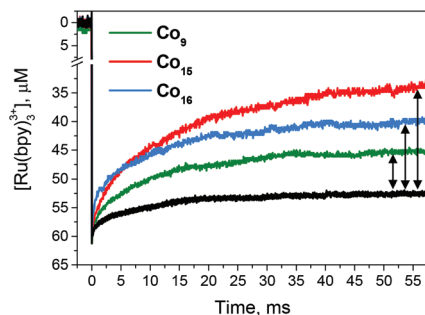


**Fig. 4** Laser flash photolysis experiments ( $\lambda_{\text{exc}} = 355$  nm) in aqueous phosphate buffer (pH 8) containing 5 mM  $\text{S}_2\text{O}_8^{2-}$ , 50  $\mu\text{M}$   $\text{Ru}(\text{bpy})_3^{2+}$  (black trace), and 1  $\mu\text{M}$   $\text{Co}_9$  (green trace), 0.5  $\mu\text{M}$   $\text{Co}_{15}$  (red trace), and 0.5  $\mu\text{M}$   $\text{Co}_{16}$  (blue trace). The amount of  $\text{Ru}(\text{bpy})_3^{3+}$  reduced by the catalyst in the time lag of the experiment (indicated by vertical double arrows) is 7.5  $\mu\text{M}$  for  $\text{Co}_9$ , 16  $\mu\text{M}$  for  $\text{Co}_{15}$  and 10  $\mu\text{M}$  for  $\text{Co}_{16}$ .

is not changed, and remains constant, even after aging of the Co-POM solutions up to three hours. This behavior is very different from what was observed for the parent  $[\text{Co}_4(\text{H}_2\text{O})_2(\text{PW}_9\text{O}_{34})_2]^{10-}$ , where a steady increase of the photo-induced ET rate occurs in a timescale of 90 minutes, thus indicating the conversion of the WOC to a more reactive ET donor over time.<sup>14</sup>

In this case, the constant value of the ET kinetics speaks against a progressive leaching of Co(II) aqua ions, that would result in a major abatement of the ET rate, as Co(II) aqua ions are inert with respect to hole-scavenging in the experimental timeframe of observation.<sup>14</sup>

Multi-hole accumulation upon sequential ET under photo-irradiation (eqn (5)), has been confirmed by flash photolysis studies using a sub-stoichiometric WOC solution, while monitoring the  $\text{Ru}(\text{bpy})_3^{2+}$  bleach recovery in an extended time window of ca. 60 ms (Fig. 4). In such a timescale, and adjusting the Co-POM concentration in terms of the overall cobalt content (in a range of 8–9  $\mu\text{M}$ ),  $\text{Co}_9$ ,  $\text{Co}_{15}$  and  $\text{Co}_{16}$  were found to react with 7.5, 32 and 20  $\text{Ru}(\text{bpy})_3^{3+}$  equivalents, respectively, corresponding to ca. 0.8 (for  $\text{Co}_9$ ), 2.1 (for  $\text{Co}_{15}$ ) and 1.2 (for  $\text{Co}_{16}$ ) average oxidation steps per cobalt center.

It is noteworthy that while a one-electron oxidation of the cobalt-core is apparent for  $\text{Co}_9$  and  $\text{Co}_{16}$ , the peak value of 2.1 ET processes resulting for  $\text{Co}_{15}$  indicates an overall Co(II) to Co(IV) redox change of the POM cobalt centers under photo-irradiation. The  $\text{Co}_{15}$  unique behavior, compared to the other high nuclearity Co-POMs, can be ascribed to its specific structural feature, with six satellite  $\text{Co}^{\text{II}}(\text{H}_2\text{O})_5$  groups grafted on the outer POM surface and a POM embedded cluster of three  $\{\text{Co}_3(\mu\text{-OH})(\text{H}_2\text{O})_3\}$  triads (Fig. 1). In this asset, the POM scaffold is expected to boost ET kinetics of the grafted Co(II) aqua ions as well as of the inner core.<sup>11</sup> \*\*\* Moreover,  $\text{Co}_{15}$  displays 39 terminal waters coordinated to the cobalt centers, that are a proof of the broad WOC accessibility and favor the multi-

\*\*\* ET in a  $\mu\text{s}$  time domain was observed for a Co-POM with an embedded Co(II) ( $\text{H}_2\text{O}$ ) moiety.

hole accumulation mechanism by the proton-coupled electron transfer (PCET) step.<sup>36</sup> Co(IV)-oxo groups, that form upon two sequential PCET steps from Co(II)-aquo moieties, have been indicated as the competent oxygen evolution sites of cobalt oxide WOCs.<sup>37</sup> Therefore, the fast generation of Co(IV) sites, as observed for  $\text{Co}_{15}$ , is expected to play a key role for WOC performance in terms of the oxygen evolution kinetics.

### Oxygen evolving catalysis

Photo-assisted oxygen evolution by the Co-POMs under investigation has been addressed under turnover conditions within the  $\text{Ru}(\text{bpy})_3^{2+}/\text{S}_2\text{O}_8^{2-}$  sacrificial cycle, in 20 mM phosphate buffer, pH 8 (Table 3). In all cases, the oxygen evolution kinetics show a well behaved profile, with no induction period as oxygen production is registered in the immediate contingency of illumination, with a steep initial rate ( $R_0$  calculated at <10% conversion), and levelling off to a plateau yield (up to 11% persulfate conversion) after ca. 30–60 minutes of irradiation (Fig. S10 in the ESI†). UV-Vis analysis of the spent reaction mixture (Fig. S11 in the ESI†) is consistent with an irreversible degradation of the ruthenium photosensitizer, which is thus responsible for the switching off of the photo-assisted catalysis.<sup>5,22–24</sup> Inspection of data in Table 3 points to addressing of the Co-POM activity in terms of their photo-assisted WOC performance, by comparing the overall oxygen productivity and the initial oxygen evolution rate  $R_0$  as a function of the POM concentration, and of the total Co loading (Table 3:  $[\text{Co}] = 19\text{--}147$   $\mu\text{M}$ ,  $[\text{Ru}(\text{bpy})_3^{2+}] = 1$  mM,  $[\text{S}_2\text{O}_8^{2-}] = 5$  mM).

Under the conditions explored, the WOC performance follows the trend  $\text{Co}_{15} \sim \text{Co}_{16} > \text{Co}_9$ , which turns out to be in line with the flash photolysis results (compare rate *versus* cobalt concentration in Fig. 3 and S10†). In particular, a linear

**Table 3** Photo-assisted oxygen production by Co-POMs within a  $\text{Ru}(\text{bpy})_3^{2+}/\text{S}_2\text{O}_8^{2-}$  sacrificial cycle.<sup>a</sup> Estimated errors from experiments run in duplicate:  $\pm 0.05$   $\mu\text{mol}$   $\text{O}_2$  in the total production of oxygen, and  $\pm 0.1$   $\mu\text{mol s}^{-1}$  for the  $R_0 \times 10^3$

#	Co-POM, $\mu\text{M}$ ( $[\text{Co}]^b$ , $\mu\text{M}$ )	$\mu\text{mol O}_2$ (TON) <sup>c</sup>	$R_0 \times 10^3$ , <sup>d</sup> $\mu\text{mol s}^{-1}$ (TOF $\times 10^3$ $\text{s}^{-1}$ ) <sup>e</sup>
1	$\text{Co}_9$ , 6.60 (58)	1.0 (10)	0.5 (5.0)
2	$\text{Co}_9$ , 16.33 (147)	1.3 (5.3)	1.1 (4.5)
3	$\text{Co}_{15}$ , 1.27 (19)	2.0 (105)	0.8 (42)
4	$\text{Co}_{15}$ , 3.86 (58)	3.1 (53)	1.2 (21)
5 <sup>f</sup>	$\text{Co}_{15}$ , 9.80 (147)	4.1 (28)	2.8 (19)
6	$\text{Co}_{16}$ , 3.62 (58)	2.0 (37)	1.3 (24)
7	$\text{Co}_{16}$ , 9.19 (147)	3.9 (28)	3.0 (22)

<sup>a</sup> In all reactions: 15 ml of a 20 mM phosphate buffered solution (pH 8) containing  $\text{Ru}(\text{bpy})_3^{2+}$  (1 mM),  $\text{S}_2\text{O}_8^{2-}$  (5 mM) and  $\text{Co}_9$ ,  $\text{Co}_{15}$  or  $\text{Co}_{16}$ . Irradiation with a tungsten lamp (cut-off filter at 375 nm, power density 90  $\text{mW cm}^{-2}$ ). <sup>b</sup> Total cobalt concentration. <sup>c</sup> TON = turnover number defined as  $\mu\text{mol O}_2$  per  $\mu\text{mol}$  WOC, determined after 1 h irradiation, persulfate conversion yield is in the range of 3–11%. <sup>d</sup>  $R_0$  initial rate of  $\text{O}_2$  production determined in the first 5 minutes of reaction. <sup>e</sup> TOF = turnover frequency defined as the maximum rate of  $\text{O}_2$  production (expressed in  $\mu\text{mol s}^{-1}$ ) over the  $\mu\text{mol}$  of WOC. <sup>f</sup> Quantum yield = 0.055 with monochromatic LED illumination ( $\lambda = 450$  nm, photon flux =  $2.63 \times 10^{-8}$  einstein per s).

dependence on the Co-POM concentration is observed both for the primary ET kinetics (up to 100  $\mu\text{M}$ , Fig. 3) and for the oxygen evolution kinetics (up to 10  $\mu\text{M}$ , Fig. S10<sup>†</sup>). This observation is consistent with the molecular nature of the competent WOC, and speaks against any major structural leaching of Co(II) ions under the conditions adopted (see further discussion). The best performing  $\text{Co}_{15}$  displays a remarkable activity at a  $\mu\text{M}$  cobalt concentration (entry 3 in Table 3,  $[\text{Co}_{15}] = 1.27 \mu\text{M}$ , total  $[\text{Co}] = 19 \mu\text{M}$ , 20 mM phosphate buffer pH 8), with a turnover number, TON, up to 100, and a turnover frequency, TOF =  $42 \times 10^{-3} \text{ s}^{-1}$ , in line with previous observations,<sup>20</sup> while the current literature benchmark,  $[\text{Co}_4(\text{H}_2\text{O})_2(\text{VW}_9\text{O}_{34})_2]^{10-}$ , is reported to reach up to  $4 \text{ s}^{-1}$  in 80 mM borate buffer<sup>16</sup> (compare entries 3 and 2 in Table S3 in the ESI<sup>†</sup>).

The quantum yield<sup>5</sup> associated with oxygen production by  $\text{Co}_{15}$  under photoirradiation with monochromatic emitting LEDs ( $\lambda = 450 \text{ nm}$ , photon flux =  $2.63 \times 10^{-8}$  einstein per s) turns out to be  $\Phi = 0.055$ . This value has been determined at a higher catalyst concentration to maximize the rate and the amount of the evolved oxygen (entry 5 in Table 3,  $[\text{Co}_{15}] = 16.33 \mu\text{M}$ ,  $[\text{Co}] = 147 \mu\text{M}$ , 20 mM phosphate buffer pH 8). Quantum yields associated with the use of cobalt substituted polyoxotungstates in  $\text{Ru}(\text{bpy})_3^{2+}/\text{S}_2\text{O}_8^{2-}$  sacrificial cycles have been reported in a few cases, using diverse buffers, pH, and illumination sources, with values up to  $\Phi = 0.34$  (Table S4<sup>†</sup>). Our data provide a direct comparison with Co(II) aquo-ions ( $\Phi = 0.11$ ,  $\lambda = 450 \text{ nm}$ , photon flux =  $1.58 \times 10^{-7}$  einstein per s,  $[\text{Co}] = 72 \mu\text{M}$ , borate buffer, pH 8)<sup>38</sup> as it turns out that higher-nuclearity Co-POMs have a rather distinct behavior with respect to POM-based analogues and to what are generally invoked as a contamination impurities,  $\text{Co}^{2+}$  ions and cobalt-oxide nanoparticles (Table S4<sup>†</sup>).

### Tracing the fate of Co-POMs after oxygenic turnover

As part of the life-cycle analysis of the high nuclearity Co-POMs, we have addressed their possible structural modification during photoirradiation, after oxygen evolution.

To this aim,  $\text{Co}_9$ ,  $\text{Co}_{15}$  and  $\text{Co}_{16}$  were recovered from the spent reaction mixtures (entries 2, 5 and 7 in Table 3) by precipitation with  $\text{Ru}(\text{bpy})_3^{2+}$  added in excess.<sup>†††</sup> In all cases, the FT-IR spectra of the isolated complexes show the expected absorption bands ascribed to a Co-POM species, where only modest wavenumber shifts are observed with respect to the pristine catalyst, likely ascribed to the solid state counterion interactions (Fig. S12–S14 in the ESI<sup>†</sup>).

Further evidence has been acquired by means of XAS spectroscopy, which is emerging as a reference technique to dissect redox changes and evolution of the coordination sphere of competent WOCs.<sup>39–42</sup> In particular, this technique has been used to confirm the POM-based structural features of

$[\text{Co}_4(\text{H}_2\text{O})_2(\text{PW}_9\text{O}_{34})_2]^{10-}$ , after oxygen evolution upon reaction with  $\text{Ru}(\text{bpy})_3^{3+}$ .<sup>39</sup> The XANES spectra, at the cobalt K-edge, are reported in Fig. 5 for the pristine Co-POMs (crystalline powders, black traces), for their solid state ionic adducts with  $\text{Ru}(\text{bpy})_3^{2+}$  (blue traces) and for the spent reaction solutions (total  $[\text{Co}] = 147 \mu\text{M}$ , in 20 mM phosphate buffer, pH 8, red traces). The superimposed edge position of  $[\text{Co}^{\text{II}}(\text{H}_2\text{O})_6](\text{NO}_3)_2$ , used as a reference (black dotted trace in Fig. 5 top), that overlaps with that of the pristine Co-POMs as crystalline powder samples (black traces in Fig. 5), confirms the Co(II) oxidation state observed in the crystallographic structures of the polyanions.<sup>39</sup> Identical edges are recorded for the solid state adducts of the Co-POMs with  $\text{Ru}(\text{bpy})_3^{2+}$  (blue traces in Fig. 5) confirming the Co(II) oxidation state in the POM adduct and the innocent role of the photosensitizer in its ground state interaction with the Co-POM catalysts. After photoirradiation and oxygen evolution, the spent reaction mixture (red traces in

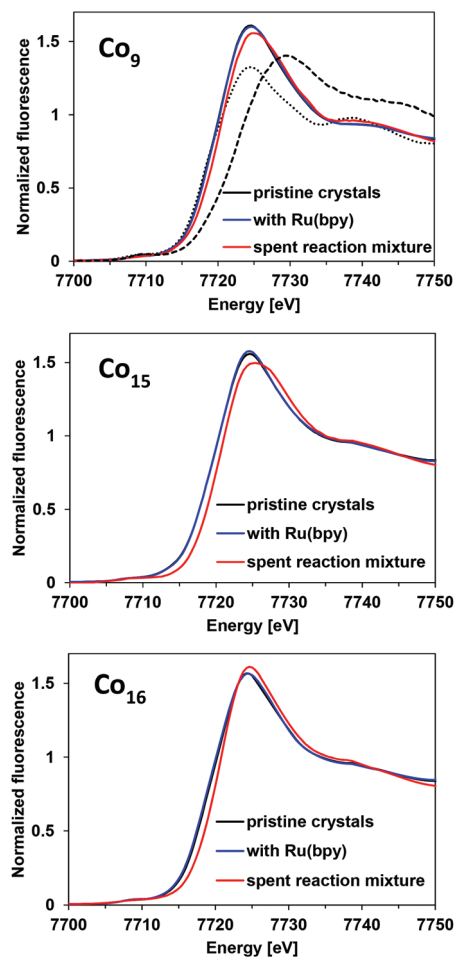


Fig. 5 XANES spectra at the cobalt K-edge. Black traces: pristine crystals of Co-POMs (solid samples); blue traces: adducts of Co-POMs with  $\text{Ru}(\text{bpy})_3^{2+}$  (solid samples); red traces: spent reaction mixtures (solution samples,  $[\text{Co}] = 147 \mu\text{M}$  in 20 mM phosphate buffer, pH 8). In the first panel  $[\text{Co}^{\text{II}}(\text{H}_2\text{O})_6](\text{NO}_3)_2$  and  $\text{Co}^{\text{III}}$ -oxide reference spectra are shown with dotted and dashed lines respectively (both from ref. 37).

<sup>†††</sup>This analysis is aimed at revealing possible rearrangements of POM based species; however, the possibility that some species derived from the Co-POMs may not be precipitated from the reaction mixture could be considered.



Fig. 5) reveals an edge shift of the XANES spectrum that is consistent with a slight increase of the average oxidation state of cobalt to about +2.2.<sup>39</sup> This observation has some important implications: (i) it rules out the structural leaching of Co(II) aqua ions;<sup>39</sup> (ii) it rules out the irreversible formation of Co<sup>III</sup>-oxide colloids as competent WOC of the sacrificial cycle (compare with the dashed line reference in Fig. 5).<sup>39,40</sup>

While the XANES region is sensitive to the oxidation state of the metal and to the geometry in its first coordination sphere, the EXAFS part may provide structural information on the higher coordination spheres.<sup>39</sup> Fig. S15 in the ESI† reports the Fourier Transformed EXAFS of the crystalline powders of the three Co-POMs (black traces) and of their respective solid state Co-POMs/Ru(bpy)<sub>3</sub><sup>2+</sup> adducts (blue traces). No significant differences are apparent for Co<sub>9</sub> and Co<sub>15</sub>, suggesting that the coordination geometry of the Co(II) sites remains unchanged. Indeed, the distances and coordination numbers obtained from the simulations fit very well to the crystal structure (Table S1 in the ESI†). On the other hand, in the case of Co<sub>16</sub> (Fig. S15† bottom) a slight variation between the EXAFS pattern of the crystalline powder (black trace) and of the Co<sub>16</sub> adduct with Ru(bpy)<sub>3</sub><sup>2+</sup> (blue trace) is ascribed to the absence of Co–P distances in the latter case (the coordination number changes from 1.5 in Co<sub>16</sub> crystalline powder to 0.1 in the Co<sub>16</sub> with Ru(bpy)<sub>3</sub><sup>2+</sup>, Fig. S15 and Table S1†). This suggests the occurrence of water exchange equilibria, involving the phosphate anions of the Co<sub>16</sub> core, once dissolved in solution.

Registration of the EXAFS part of the spectra for the three Co-POMs under photocatalytic conditions is experimentally challenging due to the low Co concentration employed in photocatalytic tests. The EXAFS spectrum from the spent reaction mixture was recorded in a shorter *k*-range (*k*12) only for the Co<sub>16</sub> species (Fig. 6, S16 and Table S2 in the ESI†), since the XANES spectrum of its adduct with Ru(bpy)<sub>3</sub><sup>2+</sup> reported above was already indicating some structural rearrange-

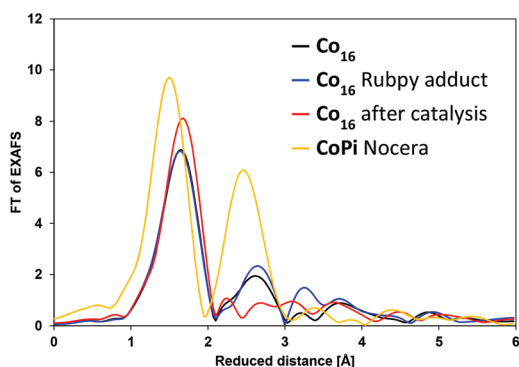


Fig. 6 Fourier transform (10–600 eV above the edge) of EXAFS spectra at the cobalt K-edge. Black trace: pristine crystals of Co<sub>16</sub> (solid samples); blue trace: adducts of Co-POMs with Ru(bpy)<sub>3</sub><sup>2+</sup> (solid samples); red trace: spent reaction mixtures (solution samples, total Co concentration 147 μM in 20 mM phosphate buffer, pH 8); yellow trace: Nocera's cobalt oxide/phosphate catalyst (CoPi).<sup>38</sup>

ment.††† This spectrum (red trace in Fig. 6) indicates some structural changes mostly related to the decrease of the number of short Co–Co vectors observed in the XRD structure at 3.03 and 3.78 Å distances as well as a decrease of the number of Co–P vectors (Table S2 in the ESI†). These structural changes may be related to the formation of open coordination sites available for substrate water binding. Our results show no indications for the formation of the previously reported catalytically active Co(III)-oxide phase (orange trace in Fig. 6 refers to Nocera's CoPi catalyst), as the 2.81 Å Co–Co distance characteristic of the CoPi catalyst<sup>39–41</sup> is absent (Table S2 in the ESI†).

## Conclusions

High nuclearity Co<sub>9</sub>, Co<sub>15</sub> and Co<sub>16</sub> polyoxometalates have been investigated as earth-abundant WOCs in combination with Ru(bpy)<sub>3</sub><sup>2+</sup>/S<sub>2</sub>O<sub>8</sub><sup>2-</sup> under visible light irradiation. Converging kinetic and spectroscopic evidence is reported to show that:

- fast and multiple electron transfer occurs from the Co-POM to photogenerated Ru(bpy)<sub>3</sub><sup>3+</sup> with up to 32 ET events in 60 milliseconds, thus enabling the oxidation state climbing of the WOC manifold from Co(II) to Co(III) and Co(IV) states;
- the oxygen evolving kinetics are registered with no induction time, and a first order dependence on the Co-POM solution concentration;
- the WOC performance follows the trend Co<sub>15</sub> ~ Co<sub>16</sub> > Co<sub>9</sub> in agreement with the flash photolysis results, indicating that fast multi-hole accumulation precludes to fast oxygen evolution under the conditions explored;
- the resident state of the Co-POMs after oxygenic turnover displays XANES spectra that are consistent with a photo-induced oxidation of the cobalt centres while retaining the POM features, thus ruling out structural leaching of Co(II) ions and evolution to cobalt oxide colloids.

As a corollary, in all cases the flash photolysis response of the Co-POMs under investigation is unique and diverse from Co(II) aqua ions and cobalt oxide materials, which is also apparent from the resulting quantum yield and molecular behaviour.

In particular Co<sub>15</sub>, displaying a multi-nuclear cobalt cluster and satellite cobalt sites on the outer POM surface, has a prominent appeal *vis-à-vis* the high number of open coordination sites, that are accessible for water binding. Indeed, EXAFS studies confirm that Co<sub>16</sub>, with no available coordination sites in its pristine state, undergoes phosphate exchange equilibria before entering the WOC regime. Besides the cobalt nuclearity, the availability of water molecules coordinated to Co(II) centers appears to be a mandatory feature to raise the cobalt oxidation

††† Co<sub>16</sub> type polyanions were previously reported to be stable under oxygen evolving conditions combined with Ru(bpy)<sub>3</sub><sup>2+</sup>/S<sub>2</sub>O<sub>8</sub><sup>2-</sup> (see ref. 20b); this apparent discrepancy with the present work could be likely associated with the different reaction conditions employed in ref. 20b (80 mM borate buffer, pH 9).



state, likely involved in the oxygenic cycle. As far as the nature of the competent oxygenic intermediate is concerned, this is the less explored aspect in this field; while in recent years several reports were aimed at developing new catalysts with improved performance, the mechanistic requisites are still not fully understood.<sup>43</sup> This is however a crucial point in the design of durable photosynthetic assemblies, which need to be conceived to meet key sustainable constraints of process optimization. These include: (i) improvement of the cobalt WOC for high photo-efficiency using solar irradiation; (ii) design of a solid state device by immobilizing the catalyst on photo-electrodes; (iii) optimization of the WOC performance in a wide pH range that will leverage the modular assembly of an integrated water splitting device; (iv) WOC application in different aqueous media, and coupling with water remediation strategies.

## Experimental

Synthesis of  $[\text{Co}_9(\text{H}_2\text{O})_6(\text{OH})_3(\text{PW}_9\text{O}_{34})_3]^{16-}$  (**Co**<sub>9</sub>),<sup>25</sup>  $[\text{Co}_6(\text{H}_2\text{O})_{30}\{\text{Co}_9\text{Cl}_2(\text{OH})_3(\text{H}_2\text{O})_9(\text{SiW}_8\text{O}_{31})_3\}^{5-}$  (**Co**<sub>15</sub>),<sup>26a</sup> and  $[\{\text{Co}_4(\text{OH})_3\text{PO}_4\}_4(\text{PW}_9\text{O}_{34})_4]^{16-}$  (**Co**<sub>16</sub>)<sup>27</sup> was performed according to the published procedures.

Cyclic voltammeteries were recorded on a BAS EC-epsilon labstation, with a glassy carbon (3 mm diameter) and a Pt wire as working and auxiliary electrodes, respectively. Ag/AgCl (3 M NaCl) was used as the reference electrode.

UV-Vis absorption spectra were recorded on a UV/Vis/NIR Jasco V-570. Emission spectra were recorded on a Horiba-Jobin Yvon Fluoromax-2 spectrofluorimeter, equipped with a Hamamatsu R3896 tube. Infrared spectra were recorded on a Nicolet 5700 FT-IR spectrophotometer using KBr pellets.

Nanosecond transient measurements were performed with a custom laser spectrometer comprised of a Continuum Surelite II Nd:YAG laser (FWHM 6–8 ns) with a frequency doubling (532 nm, 330 mJ) or tripling (355 nm, 160 mJ) option, an Applied Photophysics xenon light source including a mod. 720 150 W lamp housing, a mod. 620 power controlled lamp supply and a mod. 03-102 arc lamp pulser. Laser excitation was provided at 90° with respect to the white light probe beam. Light transmitted by the sample was focused onto the entrance slit of a 300 mm focal length Acton SpectraPro 2300i triple grating, flat field, double exit monochromator equipped with a photomultiplier detector (Hamamatsu R3896) and a Princeton Instruments PIMAX II gated intensified CCD camera, using a RB Gen II intensifier, a ST133 controller and a PTG pulser. Signals from the photomultiplier (kinetic traces) were processed by means of a LeCroy 9360 (600 MHz, 5 Gs s<sup>-1</sup>) digital oscilloscope.

Photocatalytic water oxidation tests were conducted in duplicates, in a custom-made glass reactor (solution volume = 15 mL) equipped with a steel cap, where a FOXY-R-AF probe was mounted and interfaced with Neofox Real-Time software for data collection. Illumination was performed with a tungsten lamp at 150 W, with a 375 nm filter (illumination spot of

1 cm diameter, power density of 90 mW cm<sup>-2</sup>). For quantum efficiency determination, irradiation was performed with a monochromatic LED (7 mW power) emitting at 450 nm; the photon flux was  $2.63 \times 10^{-8}$  einstein per s.

X-ray absorption data were collected at the KMC1 beamline at the BESSY II synchrotron (Helmholtz-Zentrum Berlin, Germany) at 20 K in a liquid-helium cryostat as described previously.<sup>44</sup> Data were collected in the fluorescence mode using a 13-element energy resolving Ge detector (Canberra) selecting the Mn K<sub>α</sub> fluorescence line. 10 μm Co foil was measured simultaneously in the absorption mode for energy calibration (first inflection point of the Co edge was set to 7709 eV). For the extraction of EXAFS data (conversion to *k*-space)  $E_0 = 7710$  eV was used. Other details about data analysis and simulations are provided in ref. 44.

## Acknowledgements

Financial support from Fondazione Cariparo (Starting Grant) and from Italo-Israelian Scientific & Technological Cooperation project “SOGNO”, COST actions CM1203 Polyoxometalate Chemistry for Molecular Nanoscience (PoCheMoN), CM1202 “PERSPECT-H<sub>2</sub>O” and CM1205 “CARISMA: CAlytic RoutInes for Small Molecule Activation” is gratefully acknowledged. This work was also partially funded by the Spanish Ministerio de Economía y Competitividad (MINECO) through project CTQ2015-71287-R and the Severo Ochoa Excellence Accreditation (2014–2018) SEV-2013-0319; and by the Generalitat de Catalunya (CERCA Programme and 2014 SGR-797). UK acknowledges German Science Foundation (DFG KO-2288/20-1), German Academic Exchange Council (DAAD), and Jacobs University for financial support. HD and IZ acknowledge financial support from the Berlin Cluster of Excellence on Unifying Concepts in Catalysis (UniCat, EXL 31411).

## Notes and references

- 1 K. S. Joya, Y. F. Joya, K. Ocakoglu and R. van de Krol, *Angew. Chem., Int. Ed.*, 2013, **52**, 10426.
- 2 (a) M. D. Kärkäs, O. Verho, E. V. Johnston and B. Åkermark, *Chem. Rev.*, 2014, **114**, 11863; (b) J. R. Galán-Mascarós, *ChemElectroChem*, 2015, **2**, 37.
- 3 (a) N. Cox, M. Retegan, F. Neese, D. A. Pantazis, A. Boussae and W. Lubitz, *Science*, 2014, **345**, 804; (b) J. Yano and V. Yachandra, *Chem. Rev.*, 2014, **114**, 4175; (c) M. Suga, F. Akita, K. Hirata, G. Ueno, H. Murakami, Y. Nakajima, T. Shimizu, K. Yamashita, M. Yamamoto, H. Ago and J.-R. Shen, *Nature*, 2015, **517**, 99.
- 4 Themed collection on Polyoxometalate cluster science, L. Cronin and A. Müller guest editors, *Chem. Soc. Rev.*, 2012, **22**, 7325–7648.

- 5 A. Sartorel, M. Bonchio, S. Campagna and F. Scandola, *Chem. Soc. Rev.*, 2013, **42**, 2262.
- 6 (a) H. Lv, Y. V. Geletii, C. Zhao, J. W. Vickers, G. Zhu, Z. Luo, J. Song, T. Lian, D. G. Musaev and C. L. Hill, *Chem. Soc. Rev.*, 2012, **41**, 7572; (b) G. Geisberger, S. Paulus, M. Carraro, M. Bonchio and G. R. Patzke, *Chem. – Eur. J.*, 2011, **17**, 4619.
- 7 (a) M. Quintana, A. M. López, S. Rapino, F. M. Toma, M. Iurlo, M. Carraro, A. Sartorel, C. Maccato, X. Ke, C. Bittencourt, T. Da Ros, G. Van Tendeloo, M. Marcaccio, F. Paolucci, M. Prato and M. Bonchio, *ACS Nano*, 2013, **7**, 811; (b) F. M. Toma, A. Sartorel, M. Iurlo, M. Carraro, P. Parris, C. Maccato, S. Rapino, B. Rodriguez Gonzalez, H. Amenitsch, T. Da Ros, L. Casalis, A. Goldoni, M. Marcaccio, G. Scorrano, G. Scoles, F. Paolucci, M. Prato and M. Bonchio, *Nat. Chem.*, 2010, **2**, 826.
- 8 M. W. Kanan, Y. Surendranath and D. G. Nocera, *Chem. Soc. Rev.*, 2008, **321**, 109.
- 9 (a) J. B. Gerken, J. G. McAlpin, J. Y. C. Chen, M. L. Rigsby, W. H. Casey, R. D. Britt and S. S. Stahl, *J. Am. Chem. Soc.*, 2012, **133**, 14431; (b) F. Jiao and H. Frei, *Angew. Chem., Int. Ed.*, 2009, **48**, 1841; (c) J. Rosen, G. S. Hutchings and F. Jiao, *J. Am. Chem. Soc.*, 2013, **135**, 4516; (d) S. Yusuf and F. Jiao, *ACS Catal.*, 2012, **2**, 2753; (e) N. Shi, W. Cheng, H. Zhou, T. Fan and M. Niederberger, *Chem. Commun.*, 2015, **51**, 1338; (f) M. Grzelczak, J. Zhang, J. Pfrommer, J. Hartmann, M. Driess, M. Antonietti and X. Wang, *ACS Catal.*, 2013, **3**, 383; (g) G. S. Hutchings, Y. Zhang, J. Li, B. T. Yonemoto, X. Zhou, K. Zhu and F. Jiao, *J. Am. Chem. Soc.*, 2015, **137**, 4223; (h) X. Deng, W. N. Schmidt and H. Tüysüz, *Chem. Mater.*, 2014, **26**, 6127; (i) X. Deng and H. Tüysüz, *ACS Catal.*, 2014, **4**, 3701; (j) J. D. Blakemore, H. B. Gray, J. R. Winkler and A. M. Müller, *ACS Catal.*, 2013, **3**, 2497; (k) S. Du, Z. Ren, Y. Qu, J. Wu, W. Xi, J. Zhu and H. Fu, *Chem. Commun.*, 2016, **52**, 6705.
- 10 S. Tanaka, M. Annaka and K. Sakai, *Chem. Commun.*, 2012, **48**, 1653.
- 11 F. Song, Y. Ding, B. Ma, C. Wang, Q. Wang, X. Du, S. Fua and J. Song, *Energy Environ. Sci.*, 2013, **6**, 1170.
- 12 Q. Yin, J. M. Tan, C. Besson, Y. V. Geletii, D. G. Musaev, A. E. Kuznetsov, Z. Luo, K. I. Hardcastle and C. L. Hill, *Science*, 2010, **328**, 342.
- 13 (a) J. J. Stracke and R. G. Finke, *J. Am. Chem. Soc.*, 2011, **133**, 14872; (b) J. J. Stracke and R. G. Finke, *ACS Catal.*, 2013, **3**, 1209; (c) J. J. Stracke and R. G. Finke, *ACS Catal.*, 2014, **4**, 79; (d) J. J. Stracke and R. G. Finke, *ACS Catal.*, 2014, **4**, 909; (e) S. J. Folkman and R. G. Finke, *ACS Catal.*, 2017, **7**, 7.
- 14 M. Natali, S. Berardi, A. Sartorel, M. Bonchio, S. Campagna and F. Scandola, *Chem. Commun.*, 2012, **48**, 8808.
- 15 (a) J. W. Vickers, H. Lv, J. M. Sumliner, G. Zhu, Z. Luo, D. G. Musaev, Y. V. Geletii and C. L. Hill, *J. Am. Chem. Soc.*, 2013, **135**, 14110; (b) Z. Huang, Z. Luo, Y. V. Geletii, J. W. Vickers, Q. Yin, D. Wu, Y. Hou, Y. Ding, J. Song, D. G. Musaev, C. L. Hill and T. Lian, *J. Am. Chem. Soc.*, 2011, **133**, 2068.
- 16 H. Lv, J. Song, Y. V. Geletii, J. W. Vickers, J. M. Sumliner, D. G. Musaev, P. Kögerler, P. F. Zhuk, J. Bacsá, G. Zhu and C. L. Hill, *J. Am. Chem. Soc.*, 2014, **136**, 9268.
- 17 G. Zhu, Y. V. Geletii, P. Kögerler, H. Schilder, J. Song, S. Lense, C. Zhao, K. I. Hardcastle, D. G. Musaev and C. L. Hill, *Dalton Trans.*, 2012, **41**, 2084.
- 18 P.-E. Car, M. Guttentag, K. K. Baldrige, R. Alberto and G. R. Patzke, *Green Chem.*, 2012, **14**, 1680.
- 19 (a) S. Goberna-Ferron, L. Vigara, J. Soriano-López and J. R. Galán-Mascarós, *Inorg. Chem.*, 2012, **51**, 11707; (b) S. Goberna-Ferron, J. Soriano-López, J. R. Galán-Mascarós and M. Nyman, *Eur. J. Inorg. Chem.*, 2015, 2833.
- 20 (a) R. Al-Oweini, B. S. Bassil, J. Friedl, V. Kottisch, M. Ibrahim, M. Asano, B. Keita, G. Novitchi, Y. Lan, A. Powell, U. Stimming and U. Kortz, *Inorg. Chem.*, 2014, **53**, 5663; (b) X.-B. Han, Z.-M. Zhang, T. Zhang, Y.-G. Li, W. Lin, W. You, Z.-M. Su and E.-B. Wang, *J. Am. Chem. Soc.*, 2014, **136**, 5359.
- 21 J. Soriano-López, S. Goberna-Ferron, L. Vigara, J. J. Carbó, J. M. Poblet and J. R. Galán-Mascarós, *Inorg. Chem.*, 2013, **52**, 4753.
- 22 (a) M. Orlandi, R. Argazzi, A. Sartorel, M. Carraro, G. Scorrano, M. Bonchio and F. Scandola, *Chem. Commun.*, 2010, **46**, 3152; (b) M. Natali, M. Orlandi, S. Berardi, S. Campagna, M. Bonchio, A. Sartorel and F. Scandola, *Inorg. Chem.*, 2012, **51**, 7324.
- 23 M. Natali, F. Puntoriero, C. Chiorboli, G. La Ganga, A. Sartorel, M. Bonchio, S. Campagna and F. Scandola, *J. Phys. Chem. C*, 2015, **119**, 2371.
- 24 R. Al-Oweini, A. Sartorel, B. S. Bassil, M. Natali, S. Berardi, F. Scandola, U. Kortz and M. Bonchio, *Angew. Chem., Int. Ed.*, 2014, **53**, 11182.
- 25 J. R. Galán-Mascarós, C. J. Gómez-García, J. J. Borrás-Almenar and E. Coronado, *Adv. Mater.*, 1994, **6**, 221.
- 26 (a) B. S. Bassil, S. Nellutla, U. Kortz, A. C. Stowe, J. van Tol, N. S. Dalal, B. Keita and L. Nadjo, *Inorg. Chem.*, 2005, **44**, 2659; (b) B. Keita, U. Kortz, L. R. Brudna Holzle, S. Brown and L. Nadjo, *Langmuir*, 2007, **23**, 9531.
- 27 M. Ibrahim, Y. Lan, B. S. Bassil, Y. Xiang, A. Suchopar, A. K. Powell and U. Kortz, *Angew. Chem., Int. Ed.*, 2011, **50**, 4708.
- 28 (a) A. Montellano López, M. Natali, E. Pizzolato, C. Chiorboli, M. Bonchio, A. Sartorel and F. Scandola, *Phys. Chem. Chem. Phys.*, 2014, **16**, 12000; (b) E. Pizzolato, M. Natali, B. Posocco, A. Montellano López, I. Bazzan, M. Di Valentin, P. Galloni, V. Conte, M. Bonchio, F. Scandola and A. Sartorel, *Chem. Commun.*, 2013, **49**, 9941; (c) F. Li, Y. Jiang, B. Zhang, F. Huang, Y. Gao and L. Sun, *Angew. Chem., Int. Ed.*, 2012, **51**, 2417.
- 29 C. P. Plaisance and R. A. Van Santen, *J. Am. Chem. Soc.*, 2015, **137**, 14660.
- 30 (a) M. Zhang and H. Frei, *Catal. Lett.*, 2015, **145**, 420; (b) M. Zhang, M. de Respinis and H. Frei, *Nat. Chem.*, 2014, **6**, 362; (c) T. Ling, D.-Y. Yan, H. Wang, Y. Zheng, X. Zheng, J. Mao, X.-W. Du, Z. Hu, M. Jaroniec and S.-Z. Qiao, *Nat. Commun.*, 2016, **7**, 12876; (d) H.-Y. Wang, S.-F. Huang,

- H.-Y. Chen, T.-S. Chan, H. M. Chen and B. Liu, *J. Am. Chem. Soc.*, 2016, **138**, 36.
- 31 A. M. Ullman, Y. Liu, M. Huynh, D. K. Bediako, H. Wang, B. L. Anderson, D. C. Powers, J. J. Breen, H. D. Abruña and D. G. Nocera, *J. Am. Chem. Soc.*, 2014, **136**, 17681.
- 32 M. Natali, E. Deponti, D. Vilona, A. Sartorel, M. Bonchio and F. Scandola, *Eur. J. Inorg. Chem.*, 2015, 3467.
- 33 I. A. Weinstock, *Chem. Rev.*, 1998, **98**, 113.
- 34 H. S. White, W. G. Becker and A. J. Bard, *J. Phys. Chem.*, 1984, **88**, 1840.
- 35 (a) N. D. Morris, M. Suzuki and T. E. Mallouk, *J. Phys. Chem. A*, 2004, **108**, 9115; (b) W. J. Youngblood, S.-H. A. Lee, Y. Kobayashi, E. A. Hernandez-Pagan, P. G. Hoertz, T. A. Moore, A. L. Moore, D. Gust and T. E. Mallouk, *J. Am. Chem. Soc.*, 2009, **131**, 926.
- 36 D. R. Weinberg, C. J. Gagliardi, J. F. Hull, C. F. Murphy, C. A. Kent, B. C. Westlake, A. Paul, D. H. Ess, D. G. McCafferty and T. J. Meyer, *Chem. Rev.*, 2012, **112**, 4016.
- 37 Y. Surendranath, M. W. Kanan and D. G. Nocera, *J. Am. Chem. Soc.*, 2010, **132**, 16501.
- 38 A. Genoni, G. La Ganga, A. Volpe, F. Puntoriero, M. Di Valentin, M. Bonchio, M. Natali and A. Sartorel, *Faraday Discuss.*, 2015, **185**, 121.
- 39 R. Schiwon, K. Klingan, H. Dau and C. Limberg, *Chem. Commun.*, 2014, **50**, 100.
- 40 (a) M. Risch, V. Khare, I. Zaharieva, L. Gerencser, P. Chernev and H. Dau, *J. Am. Chem. Soc.*, 2009, **131**, 6936; (b) M. Risch, F. Ringleb, M. Kohlhoff, P. Bogdanoff, P. Chernev, I. Zaharieva and H. Dau, *Energy Environ. Sci.*, 2015, **8**, 661.
- 41 M. W. Kanan, J. Yano, Y. Surendranath, M. Dinca, V. K. Yachandra and D. G. Nocera, *J. Am. Chem. Soc.*, 2010, **132**, 13692.
- 42 S. Piccinin, A. Sartorel, G. Aquilanti, A. Goldoni, M. Bonchio and S. Fabris, *Proc. Natl. Acad. Sci. U. S. A.*, 2013, **110**, 4917.
- 43 X. Sala, S. Maji, R. Bofill, J. García-Antón, L. Escriche and A. Llobet, *Acc. Chem. Res.*, 2014, **47**, 504.
- 44 M. Wiechen, I. Zaharieva, H. Dau and P. Kurz, *Chem. Sci.*, 2012, **3**, 2330.